SCIENCE CHINA
Technological Sciences

November 2012 Vol.55 No.11: 3131–3141
doi: 10.1007/s11431-012-4998-z

Numerical simulation of parachute Fluid-Structure Interaction in terminal descent

CAO YiHua[1*], WAN Kan[1], SONG QianFu[1] & SHERIDAN John[2]

[1] *School of Aeronautical Science and Engineering, Beihang University, Beijing 100191, China;*
[2] *Department of Mechanical and Aerospace Engineering, Faculty of Engineering, Monash University, VIC 3800, Australia*

Received February 21, 2012; accepted July 6, 2012; published online September 7, 2012

A numerical simulation method for parachute Fluid-Structure Interaction (FSI) problem using Semi-Implicit Method for Pressure-Linked Equations (SIMPLE) algorithm is proposed. This method could be used in both coupling computation of parachute FSI and flow field analysis. Both flat circular parachute and conical parachute are modeled and simulated by this new method. Flow field characteristics at various angles of attack are further simulated for the conical parachute model. Comparison with the space-time FSI technique shows that this method also provides similar and reasonable results.

parachute, Fluid-Structure Interaction (FSI), Semi-Implicit Method for Pressure-Linked Equations (SIMPLE) algorithm, vortex structure, flowfield topological analysis

Citation: Cao Y H, Wan K, Song Q F, et al. Numerical simulation of parachute Fluid-Structure Interaction in terminal descent. Sci China Tech Sci, 2012, 55: 3131–3141, doi: 10.1007/s11431-012-4998-z

Nomenclature

α: angle of attack
ρ: air density
V: velocity
V_∞: velocity at the inflow boundary
Γ_Φ: generalized diffusion coefficient
S_Φ: generalized source term
p: static pressure
p_∞: pressure at the inflow boundary
μ: molecular viscosity coefficient
μ_e: equivalent viscosity coefficient
C_p: pressure coefficient
ΔC_p: the pressure coefficient difference between the inner and outer canopy
K: turbulent fluctuation kinetic energy
ε: turbulent energy dissipation rate
Re: Reynolds number
φ: an angle between the canopy axis and the normal line of meridian
ψ: apex angle of conical parachute
ω: the half angle between two contiguous planes E
υ, β, θ: angles (see Figure 5)
R_f^*: dimensionless length of apex point of the cord line to the point on itself in unstretched gore state
σ_m^*, σ_u^*: dimensionless stress in canopy fabric in the longitudinal and latitudinal direction
k: shrink factor of canopy material
r^*: dimensionless bulge radius of the canopy
T^*: dimensionless force in cord line
x_f^*, z_f^*: dimensionless x and z coordinates of cord line in cylindrical coordinates
E_b, E_f: dimensionless elasticity modulus of canopy fabric and cord line

*Corresponding author (email: yihuacaocs@163.com)

1 Introduction

Parachute systems, in general, are deployed from a variety of air vehicles under many different conditions as deceleration devices. The security of aviation can be effectively improved by enhancing the capability of parachutes. In the last decades, Fluid-Structure Interaction (FSI) problem of parachute has been studied widely to meet both the public need for airliner security and military aviation. In most situations, the steadily descending phase of a parachute can be modeled as a typical incompressible flow process. Considering the flexibility and permeability of the canopy fabric, parachute systems are extremely complex. Their dynamics arise from interactions between canopy, suspension lines, load and the air around. Therefore, it is difficult to model parachute systems precisely.

Along with the progress of computing engineering, many models have been developed recently to solve the dynamics problem of parachute systems. One of the most-used models is the space-time FSI technique. It is based on the Deforming-Spatial-Domain/Stabilized Space-Time (DSD/SST) method (see refs. [1–3]), which is a moving-mesh technique. The earliest applications of these space-time FSI techniques included 2D and 3D flow computations [4, 5]. These were followed by the first application of the space-time FSI techniques to parachute modeling, reported in ref. [6] as axisymmetric computation of the inflation of a parachute. Application to parachute modeling with full 3D computations was first reported in ref. [7], in the context of a parafoil, together with a detailed description of the method and parallel implementation. The same technique was used in ref. [8] for a detailed 3D computation of a round parachute. These early parachute applications were computed with the block-iterative coupling technique (see refs. [9, 10] for the terminology and context). More robust versions of these early block-iterative techniques were introduced in ref. [9]. Also introduced in ref. [9] were the quasi-direct and direct coupling techniques, which yield more robust algorithms for the FSI computations where the structure is light and therefore more sensitive to the variations in the fluid dynamics forces (that is what we have in parachute modeling). The SST FSI technique was applied to a number of parachute simulations, including parachutes with fabric porosity [10] and the ringsail parachutes to be used with NASA's new space vehicle Orion [11–13].

Besides the space-time FSI technique which is based on the DSD/SST method, there are some other FSI techniques, for example the methods used in refs. [14, 15]. In ref. [14], the immersed boundary method was used to solve the 3D parachute simulation problems. In ref. [15], the Large-Eddy Simulation method was coupled to a structural membrane to study the supersonic disk-gap-band parachutes.

The most frequently research work has focused on the simulation and analyses of flat circular parachutes using the space-time FSI technique. More work is needed to simulate more complicated parachute models, such as the conical parachute, a typical parachute widely used in aviation utilization. In this paper, a numerical method is proposed to simulate the conical parachute fluid-structure interaction (shape determination) for the first time. This new method is basically developed by following the Semi-Implicit Method for Pressure-Linked Equations (SIMPLE) algorithm proposed by Patankar and Spalding in 1972 [16]. It is programmed easily and relatively more precise than the existing algorithms at that time. Therefore, the SIMPLE method has soon become a universal method to solve Navier-Stokes equation in incompressible flow ever since it was brought out. Based on the SIMPLE method, two 3D models of a flat circular parachute and a conical parachute using a stairstep mesh generation were built up. The simulation results provided in this study also reflect the efficiency and accuracy well. The topological structures at various angles of attack for a conical parachute model are further simulated. The performance of the method qualifies itself to be an efficient method to deal with more complicated parachute systems dynamics.

This paper is organized as follows. Section 2 is devoted to the problem statement and the preparatory analysis for modeling the parachute systems. The geometric characteristics of the parachute models to be simulated are presented. The basic principles of the SIMPLE method and the development of the simulation program are introduced in Section 3. In Section 4, a flat circular parachute model is simulated by the new method. A conical parachute model is simulated in Section 5. Situations where the angle of attack is involved are further simulated. The conclusion and discussion are provided in Section 6.

2 Modeling

2.1 Geometric parameters

Two types of parachutes (flat circular parachute and conical parachute) are involved in this paper. Parameters of these two parachute models are shown in Table 1.

Since the structure of the conical parachute is relatively complicated, a top view of the parachute is provided in Figure 1.

In Figure 1, section AA′ is the symmetrical section, and section P is chosen as characteristic section. The coordinates concerned in programming are defined as in Figure 2.

Table 1 Primary parameters of model

Parachute type	Nominal diameter (m)	Vent diameter (m)	Steady velocity ($m\ s^{-1}$)	Gore number
Flat circular parachute	8.53	0.85	6.10	28
Conical parachute	6.80	0.35	6.00	24

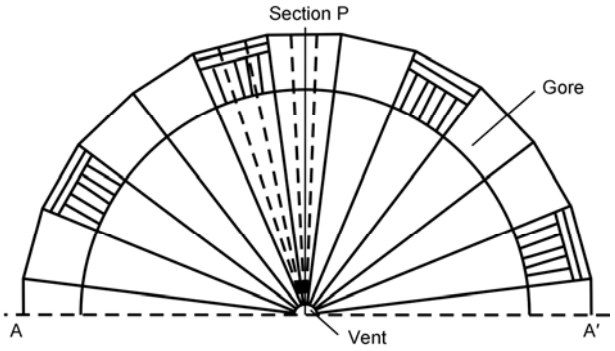

Figure 1 The top view of conical parachute model (half). AA′, Symmetrical; Section P, characteristic section.

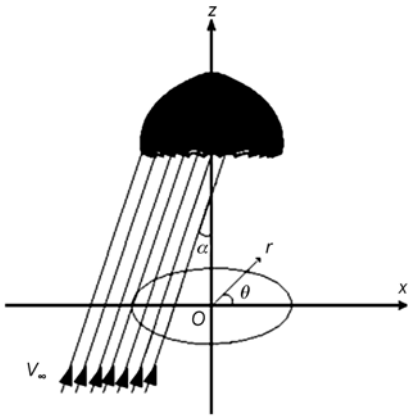

Figure 2 Coordinates definition (AA′ section).

2.2 Flow field calculation

The fluid is assumed to have constant density. The steady, incompressible, 3D turbulent Navier-Stokes equations in cylindrical coordinates are chosen as the governing equations. The turbulent Reynolds equations for conservation of mass, momentum (with θ, r, z, velocity component u, v, w), turbulent fluctuation kinetic energy K, and turbulence dissipation rate ε govern the turbulent flow of the control zone. All those equations can be expressed in the general form as eq. (1):

$$\mathrm{div}(\rho V\Phi) = \mathrm{div}(\Gamma_\Phi \mathrm{grad}\,\Phi) + S_\Phi, \tag{1}$$

where Φ represents any of the generalized dependent variables, i.e., $\Phi = 1, u, v, w, K, \varepsilon$.

The governing equations in cylindrical coordinates for parachute flow simulation are as follows:

1) Continuity equation

$$\frac{\partial u}{r\partial\theta} + \frac{1}{r}\frac{\partial(rv)}{\partial r} + \frac{\partial w}{\partial z} = 0. \tag{2}$$

2) θ-Momentum

$$\begin{aligned}&\frac{\partial}{r\partial\theta}\left(\rho u^2 - \mu_e\frac{\partial u}{r\partial\theta}\right) + \frac{1}{r}\frac{\partial}{\partial r}\left(r\rho vu - r\mu_e\frac{\partial u}{\partial r}\right)\\ &+\frac{\partial}{\partial z}\left(\rho wu - \mu_e\frac{\partial u}{\partial z}\right) = -\frac{\partial p}{r\partial\theta} + \frac{\partial}{r\partial\theta}\left[\mu_e\left(\frac{\partial u}{r\partial\theta} + \frac{2v}{r}\right)\right]\\ &+\frac{1}{r}\frac{\partial}{\partial r}\left[r\mu_e\left(\frac{\partial v}{r\partial\theta} - \frac{u}{r}\right)\right] + \frac{\partial}{\partial z}\left(\mu_e\frac{\partial w}{r\partial\theta}\right)\\ &+\frac{\mu_e}{r}\left[r\frac{\partial(u/r)}{\partial r} + \frac{\partial v}{r\partial\theta}\right] - \frac{\rho uv}{r}.\end{aligned} \tag{3}$$

3) r-Momentum

$$\begin{aligned}&\frac{\partial}{r\partial\theta}\left(\rho uv - \mu_e\frac{\partial v}{r\partial\theta}\right) + \frac{1}{r}\frac{\partial}{\partial r}\left(r\rho v^2 - r\mu_e\frac{\partial v}{\partial r}\right)\\ &+\frac{\partial}{\partial z}\left(\rho wv - \mu_e\frac{\partial v}{\partial z}\right) = -\frac{\partial p}{\partial r} + \frac{\partial}{r\partial\theta}\left[\mu_e\frac{r\partial(u/r)}{\partial r}\right]\\ &+\frac{1}{r}\frac{\partial}{\partial r}\left(r\mu_e\frac{\partial v}{\partial r}\right) + \frac{\partial}{\partial z}\left(\mu_e\frac{\partial w}{\partial r}\right) - \frac{2\mu_e}{r}\left(\frac{\partial u}{r\partial\theta} + \frac{v}{r}\right) + \frac{\rho u^2}{r}.\end{aligned} \tag{4}$$

4) z-Momentum

$$\begin{aligned}&\frac{\partial}{r\partial\theta}\left(\rho uw - \mu_e\frac{\partial w}{r\partial\theta}\right) + \frac{1}{r}\frac{\partial}{\partial r}\left(r\rho vw - r\mu_e\frac{\partial w}{\partial r}\right)\\ &+\frac{\partial}{\partial z}\left(\rho w^2 - \mu_e\frac{\partial w}{\partial z}\right) = -\frac{\partial p}{\partial z} + \frac{\partial}{r\partial\theta}\left(\mu_e\frac{\partial u}{\partial z}\right)\\ &+\frac{1}{r}\frac{\partial}{\partial r}\left(r\mu_e\frac{\partial v}{\partial z}\right) + \frac{\partial}{\partial z}\left(\mu_e\frac{\partial w}{\partial z}\right).\end{aligned} \tag{5}$$

5) Turbulent fluctuation kinetic energy equation K

$$\begin{aligned}&\frac{\partial}{r\partial\theta}\left(\rho uK - \mu_K\frac{\partial K}{r\partial\theta}\right) + \frac{1}{r}\frac{\partial}{\partial r}\left(r\rho vK - r\mu_K\frac{\partial K}{\partial r}\right)\\ &+\frac{\partial}{\partial z}\left(\rho wK - \mu_K\frac{\partial K}{\partial z}\right) = \rho G_K - \rho\varepsilon.\end{aligned} \tag{6}$$

6) Turbulent energy dissipation rate equation ε

$$\begin{aligned}&\frac{\partial}{r\partial\theta}\left(\rho u\varepsilon - \mu_\varepsilon\frac{\partial\varepsilon}{r\partial\theta}\right) + \frac{1}{r}\frac{\partial}{\partial r}\left(r\rho v\varepsilon - r\mu_\varepsilon\frac{\partial\varepsilon}{\partial r}\right)\\ &+\frac{\partial}{\partial z}\left(\rho w\varepsilon - \mu_\varepsilon\frac{\partial\varepsilon}{\partial z}\right) = \frac{\varepsilon}{K}\left(c_1\rho G_K - c_2\rho\varepsilon\right).\end{aligned} \tag{7}$$

Here

$$\begin{aligned}G_K = \frac{\mu_t}{\rho}\Bigg\{&2\left[\left(\frac{\partial u}{r\partial\theta} + \frac{v}{r}\right)^2 + \left(\frac{\partial v}{\partial r}\right)^2 + \left(\frac{\partial w}{\partial z}\right)^2\right]\\ &+\left(\frac{\partial v}{r\partial\theta} + \frac{\partial u}{\partial r} - \frac{u}{r}\right)^2 + \left(\frac{\partial u}{\partial z} + \frac{\partial w}{r\partial\theta}\right) + \left(\frac{\partial w}{\partial r} + \frac{\partial v}{\partial z}\right)^2\Bigg\},\end{aligned}$$

$$\mu_t = c_\mu\rho K^2/\varepsilon,$$

$$\mu_e = \mu + \mu_t,$$

$$\mu_K = \mu + \frac{\mu_t}{\sigma_K},$$

$$\mu_\varepsilon = \mu + \frac{\mu_t}{\sigma_\varepsilon}.$$

Considering the added $K-\varepsilon$ two-equation turbulent model, three new coefficients (c_1, c_2, c_μ) and two new constants $(\sigma_K, \sigma_\varepsilon)$ are inducted.

In this computational analysis, the SIMPLE algorithm is adopted to link the velocity vector V and static pressure p, which are initial variables of the flow field. The finite volume method is also used to discretize the governing differential equations. The convective terms are treated with power scheme, and the diffusive terms are treated with central difference scheme. The discretized equations then can be solved by using Alternating Direction Implicit (ADI) iteration method [14]. Staggered mesh method has been used to store the velocity u, v, w, pressure p, turbulent fluctuation kinetic energy K and turbulent energy dissipation rate ε in four different grid systems.

The computational area and boundary conditions are shown in Figure 3, and the lengths of *AG*, *BE* and *BC* are about five times nominal diameter of parachute. Body fitted grid of canopy is shown in Figure 4. In order to find the proper grid cell number, more than one spatial discretization was used for computing the flow field. The comparison showed that the results were convergent and almost did not change when the grids number exceeded 1000000. Therefore the grid cell number of the whole computational domain is about 1000000 (for example, using a (39×190×192) grid over a domain of half conical parachute model).

2.3 Structure simulation

The structure simulation method is mainly based on the method used in ref. [17]. The basic assumptions in structure simulation are:

1) The angle of attack is zero.

2) There are no rigidities in both of the canopy cloth and cord line.

3) There are the same strain and stress in all of the canopy gores and cord lines.

4) The curve of the intersection boundary between the plane E and canopy gore is one part of a circle.

5) The descending velocity is stable.

For the symmetrical characteristic of the flat circular parachute, one gore of the canopy is used for the structure simulation. Figure 5 is one of the structure model pictures.

According to the geometrical and physical conditions, the main equations were obtained.

Equations for flat circular parachute:

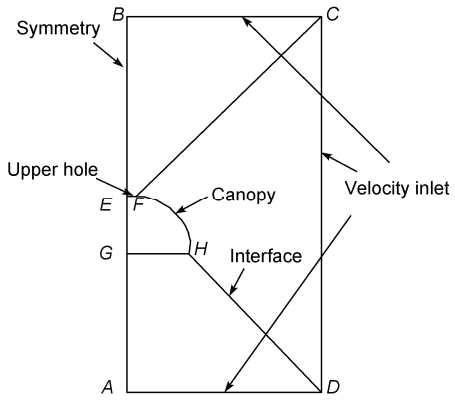

Figure 3 Computational area and boundary conditions.

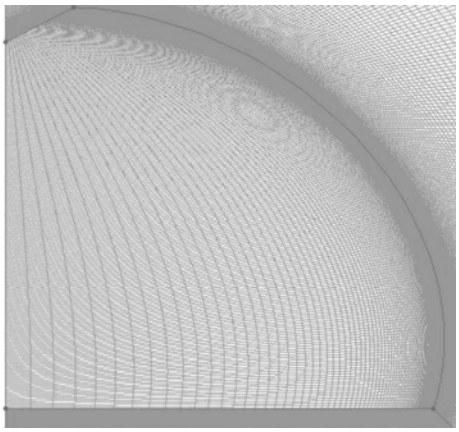

Figure 4 Body fitted grid of canopy.

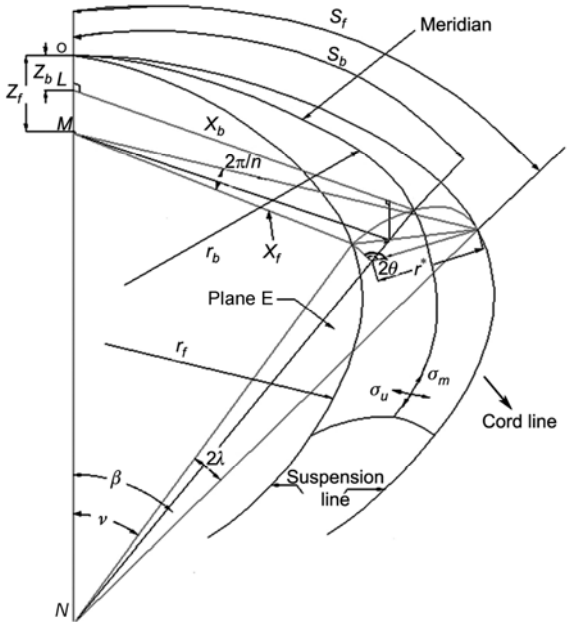

Figure 5 Structure model.

$$\frac{\mathrm{d}\varphi}{\mathrm{d}R_f^*}=\frac{\cos(\pi/N)}{\sigma_m^*}\left(1+\frac{\sigma_m^*-k\sigma_u^*}{E_b^*}\right)\left[\Delta C_p-\frac{\sigma_u^*}{r^*}\cos(\beta-\varphi)\right],$$
$$\frac{\mathrm{d}\sigma_m^*}{\mathrm{d}R_f^*}=\frac{\sigma_u^*}{r^*}\cos\frac{\pi}{N}\left(1+\frac{\sigma_m^*-k\sigma_u^*}{E_b^*}\right)\sin(\beta-\varphi), \tag{8}$$
$$\alpha r^*=\left(1+\frac{\sigma_u^*-k\sigma_m^*}{E_b^*}\right)R_f^*\sin\frac{\pi}{N}.$$

Equations for conical parachute:

$$\frac{\mathrm{d}\varphi}{\mathrm{d}R_f^*}=\frac{\cos(\theta/2)}{\sigma_m^*}\left(1+\frac{\sigma_m^*-k\sigma_u^*}{E_b^*}\right)\left[\Delta C_p-\frac{\sigma_u^*}{r^*}\cos(\beta-\varphi)\right],$$
$$\frac{\mathrm{d}\sigma_m^*}{\mathrm{d}R_f^*}=\frac{\sigma_u^*}{r^*}\cos\frac{\theta}{2}\left(1+\frac{\sigma_m^*-k\sigma_u^*}{E_b^*}\right)\sin(\beta-\varphi), \tag{9}$$
$$\alpha r^*=\left(1+\frac{\sigma_u^*-k\sigma_m^*}{E_b^*}\right)R_f^*\sin\frac{\psi}{2}.$$

Common equations:

$$\begin{aligned}
&\frac{\mathrm{d}\upsilon}{\mathrm{d}R_f^*}=\frac{2\sigma_u^*}{T^*}\left(1+\frac{T^*}{E_f^*}\right)\sin(\alpha-\lambda),\\
&\frac{\mathrm{d}T^*}{\mathrm{d}R_f^*}=2\sigma_u^*\left(1+\frac{T^*}{E_f^*}\right)\cos(\alpha-\lambda)\cos\omega,\\
&\frac{\mathrm{d}x_f^*}{\mathrm{d}R_f^*}=\left(1+\frac{T^*}{E_f^*}\right)\cos\upsilon,\\
&\frac{\mathrm{d}z_f^*}{\mathrm{d}R_f^*}=\left(1+\frac{T^*}{E_f^*}\right)\sin\upsilon.
\end{aligned} \tag{10}$$

$$\begin{aligned}
&r^*\sin\alpha=x_f^*\sin\frac{\pi}{N},\\
&\sigma_u^*=\frac{\Delta C_p r^* T^*}{2\sigma_m^* r^*\sin(\alpha-\lambda)+T^*\cos(\beta-\varphi)},\\
&\sin\lambda=\sin\frac{\pi}{N}\sin\upsilon,\\
&\sin\beta=\frac{\sin\upsilon}{\cos\lambda}\cos\frac{\pi}{N},\\
&\sin\omega=\frac{\cos(\pi/N)}{\cos\lambda}.
\end{aligned} \tag{11}$$

The method to solve the differential equations is the fourth-order Runge-Kutta algorithm. From the structural solver, the new canopy shape could be computed out for the fluid solver, and the fluid solver would provide the new canopy pressure coefficient C_p (which is defined as $C_p=\dfrac{p-p_\infty}{\frac{1}{2}\rho v_\infty^2}$) for the structural solver. The criterion for assessing the convergence of the results is: to compare the meridian shapes, when the meridian shape is almost the same in two iteration steps, the results are deemed to be converged.

More details of the basic structure simulation method can refer to ref. [17].

3 SIMPLE algorithm

The SIMPLE algorithm is a pressure correction algorithm that adopts staggered mesh method. Main steps of the SIMPLE algorithm are as follows:

1) Assume a velocity distribution, marked as u^0, v^0, w^0. Then calculate the coefficients and constant terms of the discretized momentum equations.

2) Assume a pressure field p^*.

3) Solve the two momentum equations in turn, obtain u^*, v^*, w^*.

4) Solve the pressure correction equation, obtain p'.

5) Modify the value of velocity according to p'.

6) Use the modified velocity to obtain the variable Φ that couples with velocity. If Φ brings no influence on flow field, it should be obtained after flow field converges.

7) Use the modified velocity to recalculate the coefficients and constant terms of the discretized momentum equations. Use the modified pressure field as initial value of next step of iterative computation.

The SIMPLE algorithm is an extensive algorithm in solving Navier-Stokes equation for incompressible flow. It is applicable to the flow field simulation of steady descent stage of a parachute (see ref. [16] for more details of the SIMPLE algorithm).

4 Coupling process

The two types of the inflated parachutes are similar. Since all the canopy gores are the same, the steady flow field at a zero angle of attack can be considered as axis-symmetric. The initial value of pressure coefficient difference between inner and outer surfaces is assumed to be 1.60, which would not influence the final results, because except the first step, all the other steps are obtained from the flow field simulation. Then a process of fluid-structure iteration is used to obtain the actual configuration of the steady canopy. This process can be described as shown in Figure 6.

The fluid-structure simulation method described in Figure 6 is a weak couple between the fluid and structure simulations. In the flow field simulation, the canopy shape is supposed to be not changed. In the structure simulation, the pressure distributions from the flow field simulation are assumed to be not changed. Actually, both the canopy shape and its surrounding flow have a tiny change during terminal descent. From this sense, there is a simplification for this simulation technique.

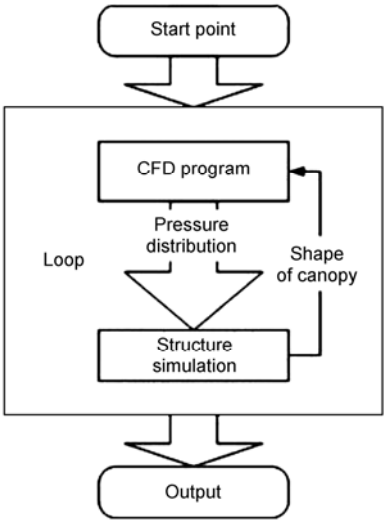

Figure 6 Flow chart of parachute simulation.

The convergence of canopy is judged through the meridian shapes in the nth and (n+1)th coupling iterations. When the tolerance of meridian shape location between the final two steps is less than 1%, the fluid-structure simulation is considered to be convergent.

5 Test problem: Flat circular parachute

After four iteration steps, Figures 7 and 8 (plotted by Rhino v3.0 software) can be plotted out. The trend of convergence can be found. The tolerance of meridian shape location in the 4th and 5th coupling iterations is less than 1%, but because using the color could not distinguish the two steps, the 5th iteration step was not plotted in Figures 7 and 8.

The final simulation model is shown in Figure 9.

Figure 10 reveals the streamlines pattern (in symmetrical axis section) for the flat circular parachute. Figure 11(a) from ref. [18] is a flow field pattern of a vented sphere. These two models have similar topological structures. The patterns of the two flow fields indicate a structural comparability between the wakes of a flat circular parachute (with a vent) and a vented sphere. However, the wake of a vented sphere shown in Figure 11(a) is obtained in a condition of $Re \leqslant 4\times10^5$, while the wake of a flat circular parachute shown in Figure 10 is obtained with $Re=3.6\times10^6$. In the condition of $Re=3.6\times10^6$, the vortices in the wake of a vented sphere would be pushed against the sphere surface instead of shedding because a strong interaction between vent-flow and outer shear layer leads to large effects on base pressure (Figure 11(b)) [18].

The main topological structure of the flat circular parachute is shown in Figure 12.

There are 4 half saddle points S' and 2 center points N_c in the flow field. Also there are 2 saddle points S along the symmetry axis. Considering the symmetry of flow field,

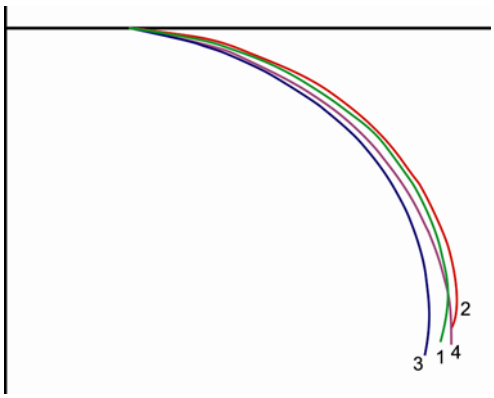

Figure 7 Change of meridian position during coupling process (flat circular parachute).

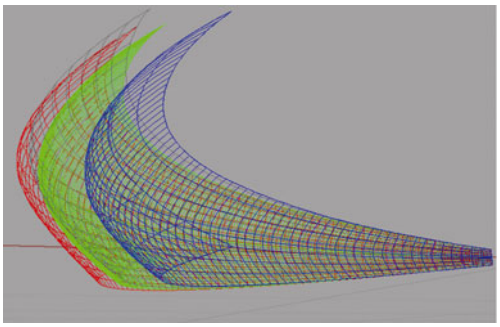

Figure 8 Change of one gore of canopy during coupling process (flat circular parachute). According to priority, steps 1 to 4 are distinguished by colors green, red, blue, and gray.

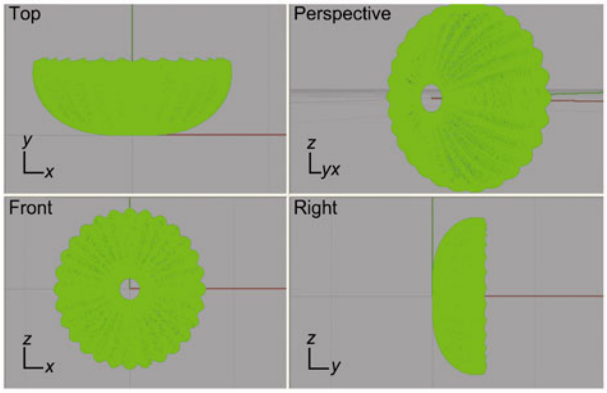

Figure 9 Flat circular parachute model.

there are 8 half saddle points, 4 center points and 2 saddle points. It obeys the topological rule [19] of flow field section:

$$\left(\sum N+\frac{1}{2}\sum N'\right)-\left(\sum S+\frac{1}{2}\sum S'\right)=1-n, \qquad (12)$$

where $n=m+1$. m is the quantity of the isolated finite section plane. In this situation, $m=2$, $n=3$.

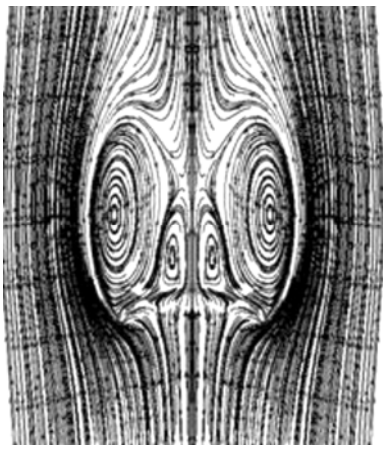

Figure 10 The streamlines pattern of our model.

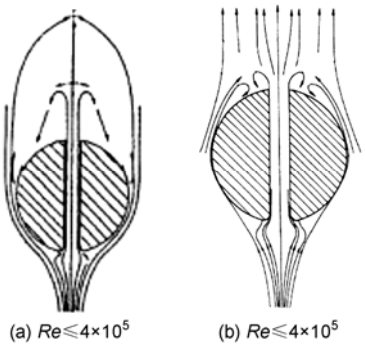

Figure 11 Flow field pattern of a vented sphere.

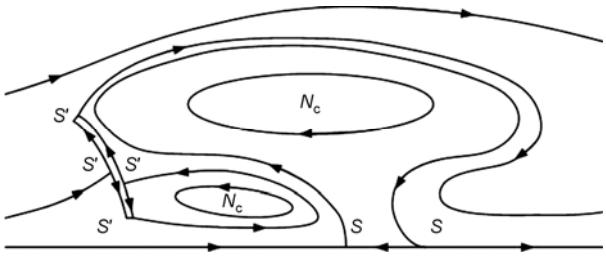

Figure 12 Topological structure of flat circular parachute flow field.

The theory of topological structure of flow field also points out that it is unsteady when the two saddle points join together. In other words, if some slight disturbances are added to this kind of flow field, the configuration of flow field can change to a totally different one. As it is described in Section 5, when angle of attack changes, the topological structure balance of parachute leeward area is broken. It reflects a dramatic change of the pattern of flow field. The process after the balance is broken is beyond the scope of this paper. Further research may be conducted in this field. Figure 13 reveals the final pressure coefficient distribution on the canopy. The three curves represent the results from three turbulence models: *S-A* model, *k-ε* model and RNG *k-ε* model. Comparatively, the non-dimensional pressure coefficient in the figure is similar to that obtained by using the parallel computing based on finite element method in ref. [20].

6 Test problem: Conical parachute

The change of meridian position during coupling process is shown in Figure 14. In Figure 14, the tolerance of meridian shape location in the 4th and 5th coupling iterations is less than 1%.

The final model of a conical parachute is shown in Figure 15.

Figure 16 reveals the flow field for the conical parachute at zero angle of attack situation ($\alpha = 0°$). We use section P in Figure 1 as feature section to monitor the main characters of the flow field.

As shown in Figure 16, the flow field configuration for the conical parachute model is similar to that of flat circular parachute model. They both exhibit two main vortices (i.e., base vortex and secondary vortex (see Figure 17).

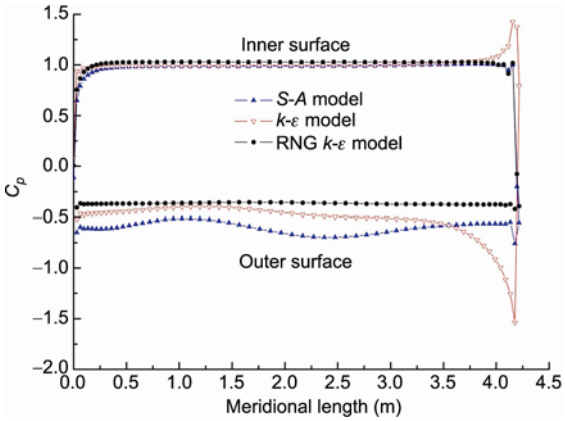

Figure 13 Pressure distribution on canopy surface.

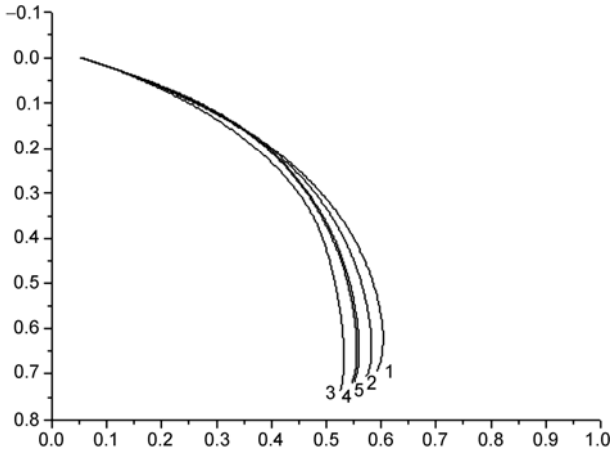

Figure 14 The change of meridian position during coupling process (conical parachute).

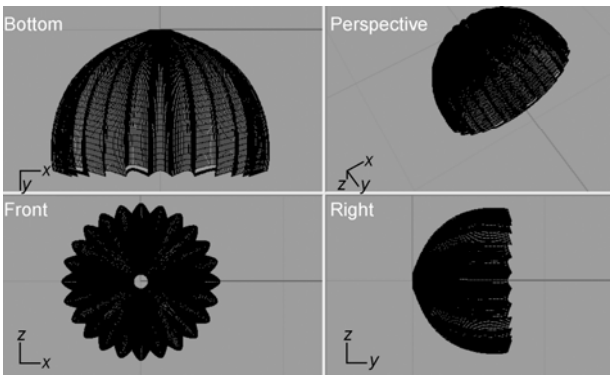

Figure 15 Conical parachute model.

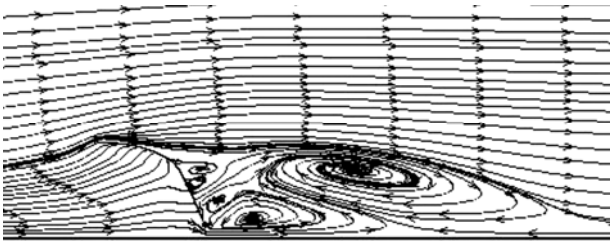

Figure 16 Flow field of conical parachute model ($\alpha = 0°$, section P).

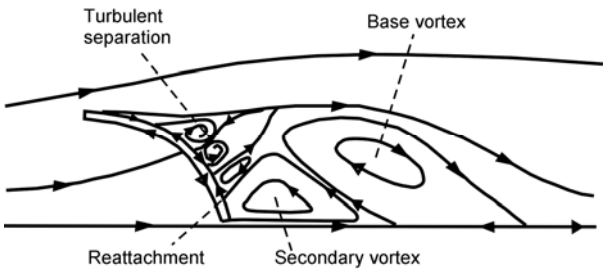

Figure 17 Topological structure of conical parachute flow field ($\alpha = 0°$, section P).

One significant difference between them is that the flow field of a conical parachute has a triangle area where turbulent separation occurs. That is because the canopy shapes of these two parachutes are different. In the conical parachute model, the larger vortex, which is a result of separation of skirt edge, tends to be further from the canopy surface than the one in flat circular parachute model. On the other hand, because the canopy surface near the vent is not perpendicular to the symmetry axis, the smaller vortex, which is a result of separation of vent border, tends to extrude the larger one. So in the triangle area enclosed by the canopy surface and the two vortices, turbulent separation flow is very complex and hard to describe (Figure 17). Further observations show that eddies in different scales are crushing and being created in this area. But these eddies are restricted in the separation zone, and barely influence the main flow outside.

Figures 18(a)–18(d) reveal the simulation results of flow field for the conical parachute model at an angle of attack of

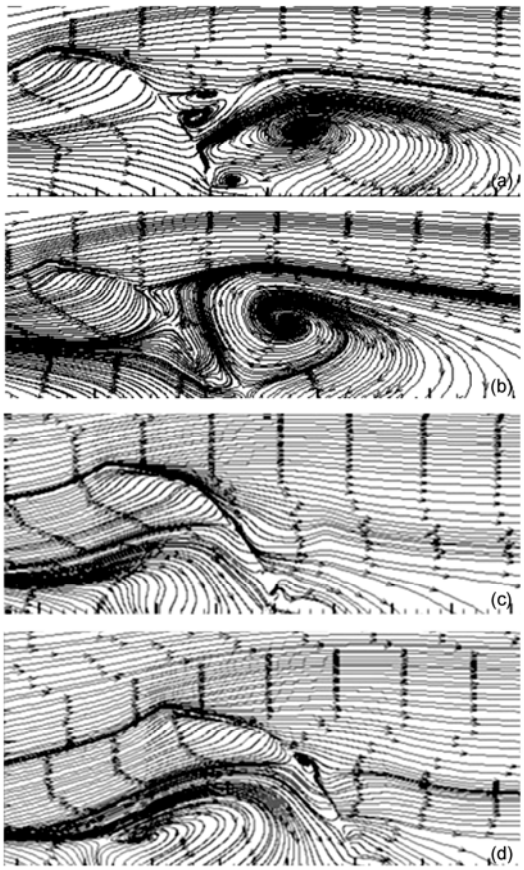

Figure 18 Flow field of conical parachute model at various α (section P). (a) $\alpha = 5°$; (b) $\alpha = 10°$; (c) $\alpha = 15°$; (d) $\alpha = 20°$.

5°, 10°, 15°, 20°, respectively. We also use section P as feature section in these figures. Changes in the flow field configuration are clearly seen from Figures 18(a) to 18(d). With the increasing of α , the eddies gradually depart from symmetry axis. And a new eddy is formed in the canopy at a greater angle of attack. Notice that the lines in these figures are not the actual streamlines. They just demonstrate the direction of velocity projections on the feature section.

The topological structure of flow field of a conical parachute model (Figure 17) is more complicated than that of a flat circular parachute model (Figure 12). Because of the interaction between vent-flow and outer layer, the base vortex is shedding away from the edge of canopy surface. The triangle area enclosed by two vortices and the canopy surface is instable. This instable structure causes a drastic change of pressure contour with the changes of the angle of attack.

The pressure contour in conical parachute model is shown in Figure 19. When angle of attack changes (Figure 19(b)), the lower pressure zones caused by the base vortex and the secondary vortex definitely depart from their original positions (Figure 19 (a)).

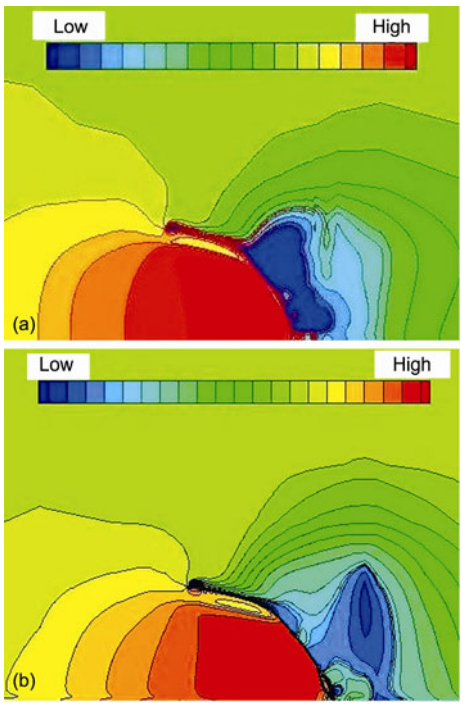

Figure 19 Pressure contours in conical parachute model (section P). (a) $\alpha = 0°$; (b) $\alpha = 5°$.

7 Vortex development

As a typical bluff body wake problem, parachute wake pattern is closely related to the *Re* number. In the case of conical parachute, the *Re* number is $Re = 2.8\times10^6$. Under this *Re* number, the separation of boundary layer in the wake of most bluff bodies is in the critical zone or supercritical zone. The most distinct characteristic of flow pattern under this *Re* number is the irregularity of the vortex shedding. However, in parachute wake, this irregularity is intentionally restrained by properly sized venting. As for $Re = 2.8\times10^6$, the flow field in parachute wake indicates a regular vortex street pattern, which is a typical characteristic of subcritical zone. In parachute wake, there are two main vortices as well as a few secondary vortices which are induced by the main ones. The generation and development of those secondary structures are one of the key causes of main vortex shedding changes.

7.1 Vortex equations

The vortex field is assumed to be limited in a bounded area τ. The fluid is incompressible and there is no divergence in the whole flow field. Then,

$$\operatorname{div}\boldsymbol{v} = 0, \quad \operatorname{rot}\boldsymbol{v} = \boldsymbol{\omega} \quad \text{in } \tau, \tag{13}$$

$$\operatorname{div}\boldsymbol{v} = 0, \quad \operatorname{rot}\boldsymbol{v} = 0 \quad \text{outside } \tau. \tag{14}$$

Because $\operatorname{div}\boldsymbol{v} = 0$, there must be a vector potential $\boldsymbol{B}$, making

$$\boldsymbol{v} = \operatorname{rot}\boldsymbol{B}.$$

Thus, in area τ,

$$\operatorname{rot}\boldsymbol{v} = \nabla\times\nabla\times\boldsymbol{B} = \nabla(\nabla\cdot\boldsymbol{B}) - \nabla^2\boldsymbol{B} = \boldsymbol{\omega}.$$

Because $\nabla\cdot\boldsymbol{B} = 0$, so

$$\nabla^2\boldsymbol{B} = -\boldsymbol{\omega}.$$

This equation has a solution

$$\boldsymbol{B} = \frac{1}{4\pi}\iiint_\tau \frac{\boldsymbol{\omega}(\xi,\eta,\zeta)}{r}\mathrm{d}\tau,$$

where

$$r = \sqrt{(x-\xi)^2 + (y-\eta)^2 + (z-\zeta)^2}.$$

Then, the velocity field can be expressed as following:

$$\begin{aligned}\boldsymbol{v} = \operatorname{rot}\boldsymbol{B} &= \frac{1}{4\pi}\nabla\times\iiint_\tau \frac{\boldsymbol{\omega}(\xi,\eta,\zeta)}{r}\mathrm{d}\tau \\ &= \frac{1}{4\pi}\iiint_\tau \nabla\times\left(\frac{\boldsymbol{\omega}}{r}\right)\mathrm{d}\tau = -\frac{1}{4\pi}\iiint_\tau \frac{\boldsymbol{r}\times\boldsymbol{\omega}}{r^3}\mathrm{d}\tau \\ &= \frac{1}{4\pi}\iiint_\tau \frac{\boldsymbol{\omega}\times\boldsymbol{r}}{r^3}\mathrm{d}\tau.\end{aligned} \tag{15}$$

This is the universal form of the induced velocity equation in vorticity field. In the 3D flow field of parachute wake, the Biot-Savart equation is used to obtain the induced velocity of vortex lines.

$$\boldsymbol{v} = \frac{\Gamma}{4\pi}\int_l \frac{\mathrm{d}\boldsymbol{l}\times\boldsymbol{r}}{r^3}. \tag{16}$$

7.2 Secondary structure in parachute wake

Secondary vortices and tertiary vortices are commonly observed in blunt-body wakes. In parachute wake, the secondary structures are widely distributed in the whole flow pattern. The vortex structure of conical parachute wake is shown in Figure 20.

In Figure 20, V1 and V2 are two main vortices. V3 is generated because of the inducement of V2. V5 is generated because of the inducement of outer shear layer stream which is a result of the shedding of V1. V4 has vorticity with the same direction as V1. According to the fluid mechanics theory on vortex shedding (see refs. [21, 22]), V4 is the remnant part of V1 after V1's shedding from canopy surface.

With zooming in to the rectangle zone in Figure 20, the more detailed pattern is shown in Figure 21.

Because of the entrainment function of V4, stream continuously flows from V5 to V4. At the same time all vorti-

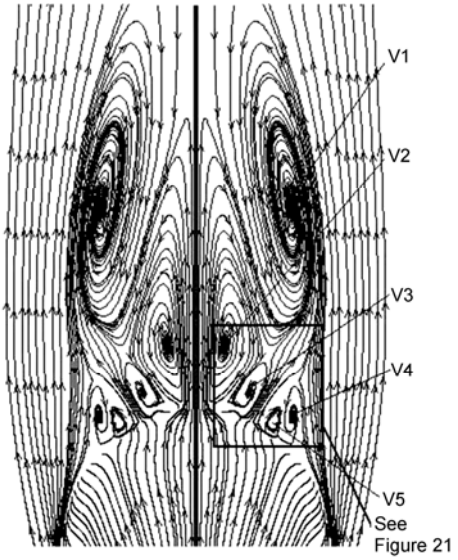

Figure 20 The vortex structure of conical parachute wake ($\alpha = 0$).

Figure 21 Zoom in view of a part of Figure 20.

ces have been formed, and the whole flow field has been in the quasi-steady stage.

Zooming in to the rectangle zone in Figure 21, more lesser structures as V6 (e.g. tertiary vortices) can be observed in Figure 22.

8 Conclusions

In this paper, the SIMPLE algorithm is applied to the parachute flow field simulation and has shown a fine synthesis capability in dealing with FSI problem of parachute models. We use this strategy to simulate a flat circular parachute model, and a conical parachute as well. Furthermore, we have obtained the patterns of conical parachute flow fields at various angles of attack for the first time. All the results have shown that the SIMPLE algorithm is a recommendable strategy in numerical simulation of parachute FSI problem.

Apparently, the new method proposed in the paper for parachute simulation is far from a mature one. It is necessary to do a lot of work to improve it.

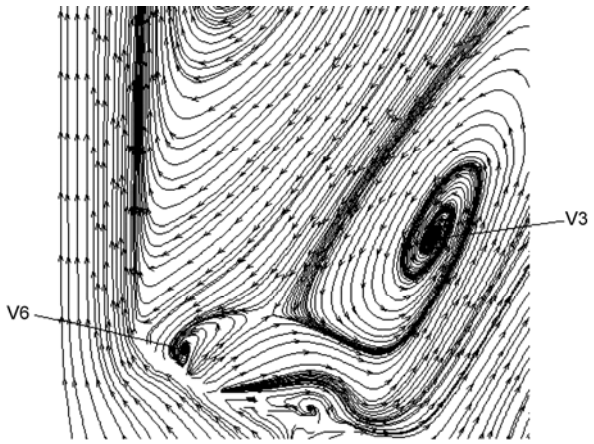

Figure 22 More lesser structures.

1) The air permeability of fabric is not considered in this paper. But it definitely has some influences on the flow field. This may be a topic in further research.

2) More studies should be carried out in future to reveal the detailed FSI process when angle of attack changes in the numerical simulation of parachute inflation.

A part of this work was supported by the National Natural Science Foundation of China (Grant No. 10577003) and Monash University of Australia.

1 Tezduyar T E. Stabilized finite element formulations for incompressible flow computations. Adv Appl Mech, 1992, 28: 1–44
2 Tezduyar T E, Behr M, Liou J. A new strategy for finite element computations involving moving boundaries and interfaces—The Deforming-Spatial-Domain/Space-Time Procedure: I. The concept and the preliminary numerical tests. Computer Meth Appl Mech Eng, 1992, 94: 339–351
3 Tezduyar T E, Behr M, Mittal S, et al. A new strategy for finite element computations involving moving boundaries and interfaces—The Deforming-Spatial-Domain/Space-Time Procedure: II. Computation of free-surface flows, two-liquid flows, and flows with drifting cylinders. Comput Meth Appl Mech Eng, 1992, 94: 353–371
4 Mittal S, Tezduyar T E. A finite element study of incompressible flows past oscillating cylinders and airfoils. Int J Num Meth Fluids, 1992, 15: 1073–1118
5 Mittal S, Tezduyar T E. Parallel finite element simulation of 3D incompressible flows-fluid-structure interactions. Int J Num Meth Fluids, 1995, 21: 933–953
6 Stein K, Benney R, Kalro V, et al. Parallel computation of parachute fluid-structure interactions. Proceedings of the 14th AIAA Aerodynamic Decelerator Technology Conference, San Francisco, AIAA-97-1505, 1997
7 Kalro V, Tezduyar T E. A parallel 3D computational method for fluid-structure interactions in parachute systems. Comput Meth Appl Mech Eng, 2000, 190: 321–332
8 Stein K, Benney R, Kalro V, et al. Parachute fluid-structure interactions: 3D computation. Comput Meth Appl Mech Eng, 2000, 190: 373–386
9 Tezduyar T E, Sathe S, Keedy R, et al. Space-Time Finite Element Techniques for computation of fluid-structure interactions. Comput Meth Appl Mech Eng, 2006, 195: 2002–2027

10 Tezduyar T E, Sathe S. Modeling of fluid-structure interactions with the Space-Time Finite Elements: solution techniques. Int J Num Meth Fluids, 2007, 54: 855–900
11 Tezduyar T E, Sathe S, Pausewang J, et al. Air-fabric interaction modeling with the stabilized space-time FSI technique. Proceedings of the Third Asian-Pacific Congress on Computational Mechanics, Kyoto, CD-ROM, 2007
12 Tezduyar T E, Sathe S, Pausewang J, et al. Interface projection techniques for fluid-structure interaction modeling with moving-mesh methods. Comput Mech, published online, 2008, doi: 10.1007/s00466-008-0261-7
13 Tezduyar T E, Sathe S, Pausewang J, et al. Fluid-structure Interaction Modeling of Ringsail Parachutes. Comput Mech, published online, 2008, doi: 10.1007/s00466-008-0260-8
14 Kim Y, Peskin C S. 3-D parachute simulation by the immersed boundary method. Comput Fluids, 2009, 38: 1080–1090
15 Karagiozis K, Kamakoti R, Cirak F, et al. A computational study of supersonic disk-gap-band parachutes using Large-Eddy Simulation coupled to a structural membrane. J Fluids Struct, 2011, 27: 175–192
16 Patankar S V. Numerical Heat Transfer and Fluid Flow. New York: Hemisphere Publishing, McGraw-Hill, 1980
17 Zhu L C. An approximate approach to calculate drag, stress and deformation of inflated flat circular parachute (in Chinese). Land Technol, 1983, (1): 143–177, translated from the paper titled as Angenäherter Berechnung der Kräfte, Spannungen und Form des Ebenen Rundkappen-Fallschirms im gefüllten Zustand. DLR(FB) 71-98 Q(W) 0860
18 Suryanaranyana G K, Prabhu, A. Effect of natural ventilation on the boundary separation and near-wake vortex shedding characteristics of a sphere. Exp Fluids, 2000, 29: 582–591
19 Tobak M, Peake D J. Topology of three-dimensional separated flows. Ann Rev Fluid Mech, 1982, 14: 61–85
20 Sahu J, Cooper G, Benney R. 3-D parachute descent analysis using coupled CFD and structural codes. AIAA-95-1580, 1995
21 Coutanceau M. On the role of high order separation on the onset of the secondary instability of the circular cylinder wake boundary. C R Acad Sci Serie II, 1988, 306: 1259–1263
22 Bouard R, Coutanceau M. The early stage of development of the wake behind an impulsively started cylinder for $40<Re<104$. J Fluid Mech, 1980, 101: 583–607